Published in final edited form as:

*Nature*. 2015 February 19; 518(7539): 431–434. doi:10.1038/nature14160.

# Structure of the key species in the enzymatic oxidation of methane to methanol

**Rahul Banerjee**[1,2], **Yegor Proshlyakov**[3], **John D. Lipscomb**[1,2], and **Denis A. Proshlyakov**[3]

[1]Department of Biochemistry, Molecular Biology & Biophysics, University of Minnesota, Minneapolis, Minnesota 55455, USA.

[2]Center for Metals in Biocatalysis, University of Minnesota, Minneapolis, Minnesota 55455, USA.

[3]Department of Chemistry, Michigan State University, East Lansing, Michigan 48824, USA.

## Abstract

Methane monooxygenase (MMO) catalyses the $O_2$-dependent conversion of methane to methanol in methanotrophic bacteria, thereby preventing the atmospheric egress of approximately one billion tons of this potent greenhouse gas annually. The key reaction cycle intermediate of the soluble form of MMO (sMMO) is termed compound Q (Q). Q contains a unique dinuclear $Fe^{IV}$ cluster that reacts with methane to break an exceptionally strong 105 kcal $mol^{-1}$ C-H bond and insert one oxygen atom[1,2]. No other biological oxidant, except that found in the particulate form of MMO, is capable of such catalysis. The structure of Q remains controversial despite numerous spectroscopic, computational and synthetic model studies[2–7]. A definitive structural assignment can be made from resonance Raman vibrational spectroscopy but, despite efforts over the past two decades, no vibrational spectrum of Q has yet been obtained. Here we report the core structures of Q and the following product complex, compound T, using time-resolved resonance Raman spectroscopy ($TR^3$). $TR^3$ permits fingerprinting of intermediates by their unique vibrational signatures through extended signal averaging for short-lived species. We report unambiguous evidence that Q possesses a bis-μ-oxo diamond core structure and show that both bridging oxygens originate from $O_2$. This observation strongly supports a homolytic mechanism for O-O bond cleavage. We also show that T retains a single oxygen atom from $O_2$ as a bridging ligand, while the other oxygen atom is incorporated into the product[8]. Capture of the extreme oxidizing potential of Q is of great contemporary interest for bioremediation and the development of synthetic approaches to methane-based alternative fuels and chemical industry feedstocks. Insight into the formation and reactivity of Q from the structure reported here is an important step towards harnessing this potential.



Correspondence and requests for materials should be addressed to D.A.P. (dapro@chemistry.msu.edu) or J.D.L. (lipsc001@umn.edu)..

**Author Contributions** R.B., Y.P. and D.A.P. developed the enhanced instrument and performed the experiments, D.A.P. analysed the data, and R.B., D.A.P. and J.D.L. designed the experiments and wrote the manuscript.

The authors declare no competing financial interests.

Online Content

Methods, along with any additional Extended Data display items and Source Data, are available in the online version of the paper; references unique to these sections appear only in the online paper.

Transient kinetic studies of sMMO have revealed eight reaction cycle intermediates, thereby providing the most comprehensive description of enzymatic $O_2$ activation and C-H bond oxidation currently available for any di-iron oxygenase[1,9–11] (Fig. 1a). It is broadly accepted that the linear increase in the decay rate constant for **Q** with concentration of methane indicates reaction between **Q** and substrates with concomitant formation of the product complex **T**. **Q** is formed in a single turnover system by mixing $O_2$-containing buffer solution with the heterocomplex of diferrous sMMO hydroxylase ($MMOH^{red}$) and regulatory B component (MMOB). In the absence of methane, the yellow **Q** has a lifetime of several seconds, accumulates in high yield, and can be trapped by rapid freeze-quench (RFQ) techniques. Several spectroscopic studies of trapped **Q** have been successful[2,3,10], but not RFQ-resonance Raman, perhaps owing to weak resonance Raman enhancement and/or photosensitivity of **Q**. To minimize photolysis, we acquired the resonance Raman spectrum of **Q** in a continuously flowing reactant stream, while at the same time extending spectral accumulation to many hours[12].

Previous studies have shown that **Q** maximizes at $\Sigma t \approx 3$ s after initiation of the reaction between $MMOH^{red}$/MMOB and $O_2$ at pH 7.0, 4 °C in the absence of substrate[1] (Extended Data Fig. 1a). Accordingly, we observe the electronic absorption spectrum of **Q** at this time in the $TR^3$ flow cell (Fig. 1b).

The absolute resonance Raman spectra of the reaction mixture at $\Delta t \approx 3$ s ($\lambda_{ex} = 351$ nm) are dominated by non-resonant vibrations of bulk solution due to the relatively low attainable enzyme concentration (0.25 mM) (Extended Data Fig. 2). Repetitive switching between $^{16}O_2$-and $^{18}O_2$-saturated oxygen streams, while maintaining the same diferrous $MMOH^{red}$/MMOB stream, eliminates minute variability between sample preparations. The $O_2$ isotope difference spectra reveal weak vibrations that involve dioxygen-derived atoms, thus identifying sMMO intermediates, while all other vibrations cancel out (Fig. 1c, trace (i), and Extended Data Fig. 2).

Two distinct oxygen vibrations were detected at $\Delta t \approx 3$ s in the absence of substrate (Fig. 1c, trace (i)): a major mode at 690 $cm^{-1}$ (identified herein by the $^{16}O$ isotopomer and the $^{16}O/^{18}O$ downshift, $\Delta^{18}O = 36$ $cm^{-1}$) and a weaker mode at 556 $cm^{-1}$ ($\Delta^{18}O = 23$ $cm^{-1}$). No noticeable laser power dependence was observed, thus excluding photochemistry under these conditions (Extended Data Fig. 3). Neither of the vibrations was observed at a long delay time ($\Delta t \approx 30$ s).

The catalytic relevance of the observed intermediate(s) was probed by mixing substrates into the reactant stream, which is expected to fully quench **Q**[1]. Accordingly, the 690 $cm^{-1}$ mode disappeared upon addition of methane or furan (Fig. 1c, traces (ii) and (iii)). A concomitant fourfold increase in the intensity of the 556 $cm^{-1}$ mode shows that this vibration arises from a different intermediate that evolves from **Q** as it reacts with substrate. The rate constants for **Q** decay with methane or furan predict a predominant accumulation of **T** at $\Delta t \approx 3$ s (ref. 1; Extended Data Fig. 1b, c). A broad near-ultraviolet electronic absorption band for **T** allows its resonance enhancement ($\lambda_{ex} = 351$ nm) (Extended Data Fig. 4). Based on substrate-induced build-up and its transient nature, the 556 $cm^{-1}$ vibration mode is assigned to **T**. The observation of the resonance Raman spectrum of **T** in the absence of substrate suggests that

the spontaneous decay of **Q** involves similar intermediates as found in the substrate mediated process.

The exceptionally large deuterium kinetic isotope effect in the reaction of **Q** with methane[8] reveals further correlation between **Q** and the 690 $cm^{-1}$ mode. This step is slowed by a factor of 50 when using $CD_4$ rather than $CH_4$ due to the large tunnelling component in the reaction coordinate[13] (Extended Data Fig. 1d). Indeed, the loss of intensity of the 690 $cm^{-1}$ vibration and the increase of the 556 $cm^{-1}$ vibration were much smaller when using $CD_4$ as substrate (Fig. 1c, trace (iv)).

An initial assignment of the structure for the di-iron cluster of **Q** can be made by comparing its resonance Raman spectrum to those of model complexes (Table 1, Extended Data Table 1). The observed frequency of 690 $cm^{-1}$ for **Q** is much less than the $\nu_{Fe=O}$ of terminal ferryl complexes[12,14]. Moreover, the $\Delta^{18}O$ shift of 36 $cm^{-1}$ for **Q** is greater than the expected value for an $Fe^{IV}$=O diatomic oscillator at this frequency. Therefore, the possibility of an isolated, terminal $Fe^{IV}$=O moiety in **Q** can be excluded (Fig. 3, panel (v)), as can be a peroxy complex, which would exhibit the $\nu_{O-O}$ at even higher frequency[15]. In contrast, the $\nu_{Fe-O}$ of end-on $Fe^{III}$-OH, $Fe^{IV}$OH and $Fe^{II}$-$O_2$ complexes appear at lower frequencies than observed here[16–18]. Protonated ligands typically exhibit a pronounced downshift upon bulk water deuteration, which we did not observe for **Q** (Fig. 1d). Indeed, the vibration frequency and $\Delta^{18}O$ isotopic shift for **Q** agree with values observed in only one class of synthetic di-iron models, namely bis-μ-oxo 'diamond core' complexes[19].

The defining feature of a diamond core structure is the presence of two vibrationally coupled μ-oxo bridges resulting in tetratomic vibrations (Table 1). This coupled motion yields a unique signature that allows discrimination of the diamond core from other structures by using the mixed isotopomer of oxygen ($^{16}O^{18}O$) (ref 19). If the diamond core comprises both oxygen atoms from $O_2$, then mixed oxygen substitution in **Q** (**Q**-$^{16}O^{18}O$) will result in a new vibration appearing symmetrically between those of the **Q**-$^{16}O_2$ and **Q**-$^{18}O_2$ (Fig. 2b, c, green). However, the absence of a diamond core or the incorporation of only one of two oxygen atoms from $O_2$ (Fig. 3, panel (iv)) will yield the same vibrational frequencies as observed for **Q**-$^{16}O_2$ and **Q**-$^{18}O_2$ with smaller $\Delta^{18}O$ (Fig. 2a–c, blue, red). Subtraction of $\nu$(**Q**-$^{16}O^{18}O$) from the average of $\nu$(**Q**-$^{16}O_2$) and $\nu$(**Q**-$^{18}O_2$) (Fig. 2c, trace (iii)) reveals a new frequency at ~673 $cm^{-1}$ in the resonance Raman spectrum of the asymmetrically labelled derivative, showing definitively that it arises from a diamond core di-iron cluster of **Q**. Notably, the new vibration also indicates that **Q** retains both oxygen atoms from $O_2$. The absence of **Q**-$^{16}O^{18}O$ vibration in the $^{16}O_2$-$^{18}O_2$ difference (Fig. 2c, trace (i)) shows that no exchange occurs between $O_2$ atoms and bulk water (Extended Data Fig. 5).

Subtraction of $\nu$(**T**-$^{16}O^{18}O$) from the average of $\nu$(**T**-$^{16}O_2$) and $\nu$(**T**-$^{18}O_2$) results in cancellation of all oxygen vibrations (Fig. 2c, trace (iii)), demonstrating that **T** inherits only one of two oxygen atoms from $O_2$. This vibration is unchanged for samples prepared in $D_2O$ (Fig. 1d), strongly suggesting that **T** does not possess a protonated bridging oxygen or terminal Fe-OH moiety, which are the only other species with similar resonance Raman vibrational fingerprints (Table 1). Thus, we assign **T** as a mono-μ-oxo-bridged structure derived from **Q** by transfer of one oxygen atom to product, as observed experimentally[8]

(Fig. 3, panel (vi)). We found no indication that labelled product is directly bound to the di-iron cluster in **T**. Together with the **Q** data, these observations allow each oxygen atom from $O_2$ to be tracked throughout the reaction cycle.

The observation that both bridging atoms in **Q** are derived from the same $O_2$ molecule has important implications for the mechanism of $O_2$ activation in sMMO. The dinuclear iron cluster in the **P** intermediate (Fig. 3, panel (i)) that precedes **Q** is predicted to possess a symmetrical *cis*-μ-1,2 peroxo bridge[20]. Proton migration in **P** facilitates O-O bond cleavage to form **Q**, which could occur either heterolytically (as in cytochrome P450)[21] or homolytically (as in some dinuclear copper-$O_2$ complexes and mimics of NO reductase)[22,23]. A heterolytic cleavage mechanism would result in formation of a water molecule from an $O_2$-derived atom (Fig. 3, panel (iv), and Extended Data Fig. 5c). Our results show that neither of the $O_2$-derived atoms is lost from the cluster, nor do we see vibrations of $O_2$-derived water bound to the iron atoms. While it is possible to formulate a mechanism for symmetrical diamond core formation by heterolytic O-O cleavage (Extended Data Fig. 5b), such a scenario would involve large asymmetric changes in the oxidation states of the cluster irons and would probably show solvent oxygen incorporation into the diamond core of **Q**, which we do not observe. Consequently, $O_2$ activation in sMMO is likely to proceed via homolytic cleavage (Fig. 3, panels (ii) and (iii), and Extended Data Fig. 5a), highlighting different mechanistic strategies of haem and non-haem enzymes for generation of potent oxygenating species.

A previous combined Mössbauer and Extended X-ray Absorption Fine Structure study of **Q** revealed an exceptionally short Fe–Fe distance[3]. The model complexes available at the time suggested that the short Fe–Fe distance could be accommodated by a bis-μ-oxo 'diamond-core' structure[3]. In recent years, other structures of **Q** have been proposed based on new synthetic model complexes[20,24]. It was found that formation of an $Fe^{IV}$=O moiety in an open-core low-spin $Fe^{IV}/Fe^{IV}$ or high-spin $Fe^{III}/Fe^{IV}$ complex resulted in major increases in reactivity compared with the low-spin closed diamond core $Fe^{IV}/Fe^{IV}$ or $Fe^{III}/Fe^{IV}$ models with the same ligand structure[24]. Contrary to several open-core proposals for **Q**[20] that developed from this finding (Fig. 3, panel (v)), we do not detect an $Fe^{IV}$=O moiety indicative of an open core in **Q**. A coupled, polyatomic vibration in **Q** shows that it does have a diamond-core structure. Consequentially, the key to the reactivity of nature's most potent oxidant is likely to come from the spin state of the cluster, putting emphasis on further synthetic work towards mimicking the high-spin nature of **Q**, while retaining the high-valent diamond core.

## METHODS

### Chemicals

All chemicals used were of the highest grade available and were purchased from Sigma-Aldrich. $^{18}O_2$ was obtained from ICON. The asymmetrically labelled oxygen isotope ($^{16}O^{18}O$) was synthesized by E. H. Appelman from Argonne National Laboratory[12]. $D_2O$ was obtained from Cambridge Isotope Laboratories.

## Biological materials

MMOH was purified from *Methylosinus trichosporium* OB3b and MMOB from a heterologous expression system in *Escherichia coli* according to purification protocols described previously[11,30]. Low molar extinction of transient intermediates compounded by the nature of the $TR^3$ experiment required a large amount of the MMOH protein, estimated to be about 30 g for the experimental results presented here, with more than half used in the instrumentation development and optimization phases.

## Sample preparation

Anaerobic solutions of MMOH in 50 mM MOPS, pH 7.0, 5% glycerol and MMOB in 50 mM MOPS, pH 7.0 were prepared in sealed vials by exchanging the headspace gas with argon while stirring on ice for 1 h. The chemical reduction of MMOH was conducted by anaerobic addition of methyl viologen (200 μM) and sodium hydrosulphite (4 mM) while stirring for 15 min at room temperature. MMOH was subsequently separated from the small molecule reducing agents by passage through a Sephadex G-25 PD-10 desalting column equilibrated in 75 mM MOPS buffer at pH 7.0 containing 5% glycerol, 0.1% Triton X-100, 200 μM $Fe(NH_4)_2SO_4$ and 2.0 mM L-cysteine (buffer A). The glycerol stabilizes the diferrous enzyme while Triton X-100 prevents protein aggregation in the flow cuvette that leads to disruption of the laser beam. The exogenous iron included in Buffer A in the form of the $Fe^{II}$-cysteine complex is used to maintain MMOH activity and does not reconstitute the protein active site[31]. Extensive controls have been carried out to ensure that it does not contribute to the observed vibrational spectra. Control stopped-flow experiments showed that neither glycerol nor Triton X-100 affected the decay rate constant for **Q**. Anaerobic MMOB was added to $MMOH^{red}$ to obtain a 1:1 MMOH active sites to MMOB ratio (480 μM). The protein was transferred to the secondary glove bag (Plas-Labs) where it was installed on the syringe infusion pump. The running enzyme syringe was continuously chilled to 4 °C using a Peltier cooling block mounted atop the syringe since $MMOH^{red}$ slowly precipitates at room temperature during the time required for a measurement (typically 1–5 h). For the experiments with deuterated solvents, the MMOH sample was exchanged by passage through the PD-10 desalting column equilibrated in buffer A prepared in $D_2O$ (pH reading was adjusted to correct for $D^+$ vs. $H^+$ concentration). The isotopic enrichment of deuterated samples is estimated at 90%. The $TR^3$ experiment was conducted at 5–6 °C to avoid freezing of the $D_2O$ buffer.

## $TR^3$ measurements

While the core design of the instrument is similar to the cryogenic $TR^3$ study described previously[12], a brief overview of the instrument and experimental design are provided to describe the extensive revisions that were required for the current study. The $TR^3$ experiment relies on active mixing of the continuous streams of $MMOH^{red}$/MMOB and oxygen-saturated buffer at a volumetric ratio of 1:1. The maximal concentration of **Q** in the absence of substrate was estimated to be 95 μM at the probe point, which arises from the 40% active fraction of MMOH[11].

Sample is delivered to a fused silica flow cuvette (25 mm long, internal cross section 0.15 × 1.5 mm, Starna Cells) where it is probed approximately 5 mm from the mixer outlet (dead

volume ~3 μl). The time resolution is achieved by varying the flow rates of the mixed stream driven by computer controlled syringe infusion pumps (high-pressure OEM modules, Harvard Apparatus). Flow rates varying between 100 μl per min and 2.5 μl per min per line result in ageing times of 1 – 36 s. The mixer with the attached flow cuvette are mounted on a translation stage driven by an actuator drive (model ZST25, Thorlabs, Inc.) via a motion control board (KFLOP, DynoMotion). This actuator maintains a constant reciprocating translation of the cuvette along the sample flow direction over a distance of ~1 mm at a speed of 0.02 mm $s^{-1}$. This limits the residence time of the slow-moving protein solution along the walls of the flow cuvette in the laser beam. Scattering from the near-wall areas of the cell was rejected optically. The temperature of gas is maintained at 4 °C by re-heating the nitrogen stream from a dry-ice/ethanol bath with a two-channel temperature controller (Model 34, Cryocon). In addition, the temperature of the core mixing chamber is further controlled by attached miniature Peltier cells. All wetted surfaces in the $TR^3$ setup are comprised of protein-compatible PEEK, PTFE (in anaerobic atmosphere), fused silica and glass.

The oxygen-saturated buffer was prepared by addition of 1 ml of $O_2$ gas to 6 ml of argon-sparged anaerobic buffer at room temperature in a 10 ml gastight syringe. During operation of the $TR^3$ experiment, the oxygen-saturated buffers were automatically and repeatedly purged and switched from one isotope to the other using computer-controlled actuated HPLC valves (Upchurch Scientific & Rheodyne, IDEX Health & Science). Resonance Raman spectra were collected in 4–12 pairs of oxygen isotope runs in the course of a single $TR^3$ experiment to randomize the non-isotopic variations in the sample composition. Results of three to eight separate experiments performed over the course of several months using different enzyme preparations were averaged together, taking into account normalization of resonance Raman intensity.

Methane saturated buffer ($CH_4$ or $CD_4$) was prepared in an identical fashion to the oxygen saturated buffer. The furan substrate was introduced by adding a calculated volume to the reduced protein sample.

Excitation in the near-ultraviolet (351 nm argon laser line, Coherent, model Innova 300) was used to maximize resonance Raman enhancement and eliminate possibility of interference from porphyrins. The laser power was typically 60 mW and was reduced down to 15 mW during power dependence studies. At a flow rate of 10 μl per min and full laser power an estimated 6,700 photons were absorbed per molecule of **Q**.

Acetone injected into the flow cell was used as a standard for calibration of the resonance Raman shifts and was subsequently purged with anaerobic buffer. Quantitative analysis of spectral changes over the reaction time or with substrate/solvent substitution was facilitated by normalization to the intensity of a 756 cm−1 protein mode as an internal standard. Further details of the spectral analysis are described in the supplementary text of reference 12.

## Extended Data

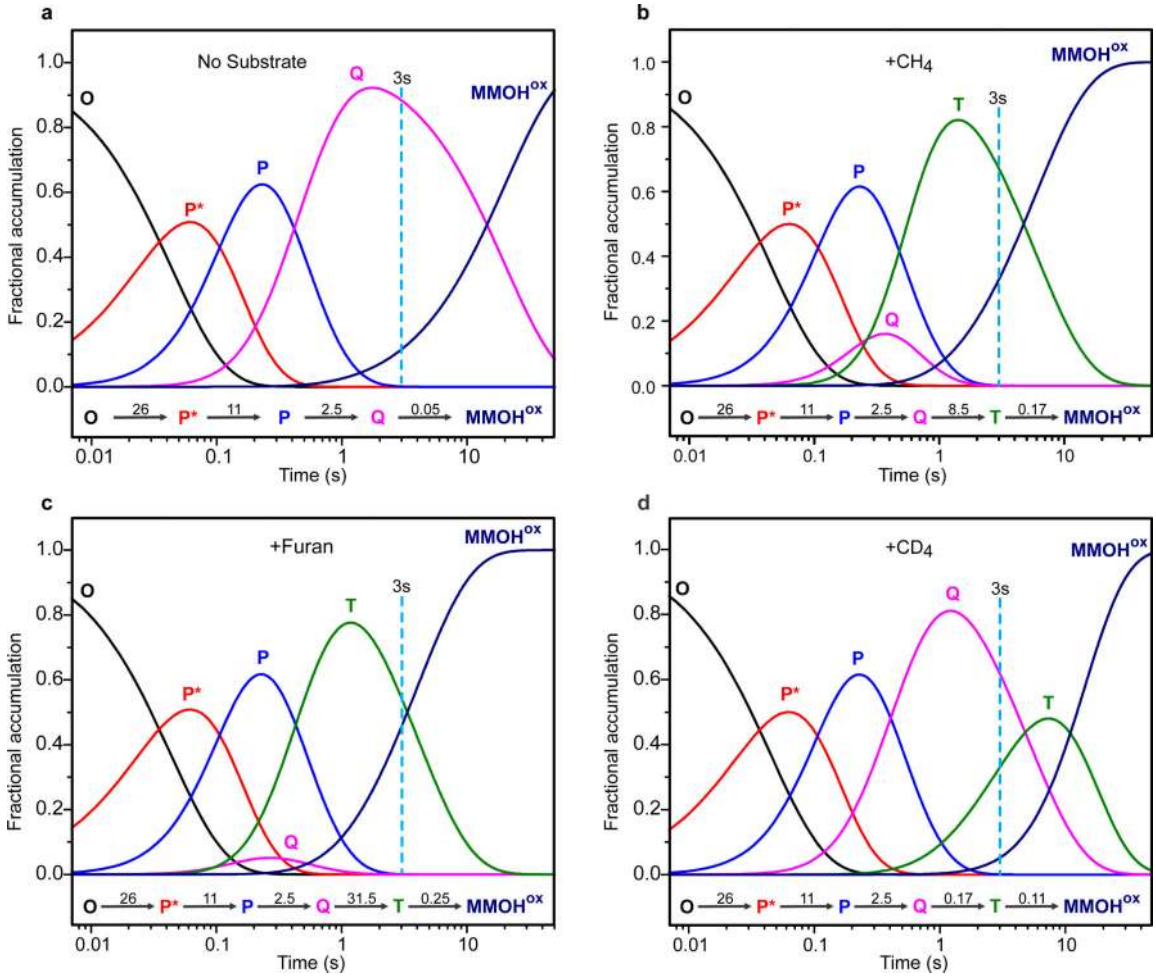


**Extended Data Figure 1. Speciation plots of the sMMO reaction with $O_2$**

Plots were computed using known rate constants of the catalytic steps[1,8,32,33] for the following conditions. **a**, No added substrate, **b**, presence of 0.45 mM $CH_4$, **c**, presence of 3.5 mM furan and **d**, presence of 0.45 mM $CD_4$ at pH 7.0, 4 °C. Rate constants used in simulation of individual conditions are shown for each step. All rate constants are first order ($s^{-1}$) except for the **Q** to **T** step, which is first order in both **Q** and substrate ($M^{-1}$ $s^{-1}$) but is given as a pseudo first order constant for the current substrate concentration. The rate constant for the formation of intermediate **O** (oxygen binding) is unknown, but it is assumed to be fast based upon typical rates for metalloenzymes of the MMO type. It is irreversible because the rate constant of the next step (**O** → **P***) is independent of $O_2$ concentration.

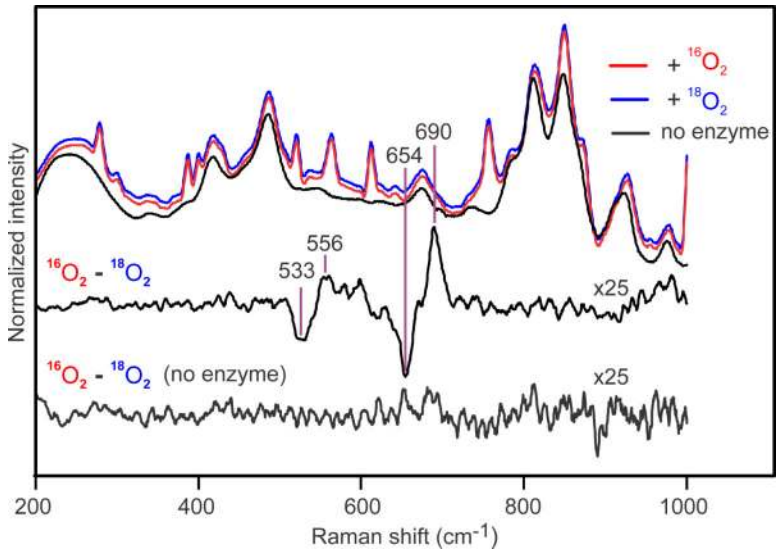


**Extended Data Figure 2. Absolute TR$^3$ spectra of the sMMO reaction with $O_2$**

Top, reaction using $^{16}O_2$-containing buffer (blue), $^{18}O_2$-containing buffer (red) or buffer background in the absence of MMOH/MMOB (black). Middle, $^{16}O_2$ – $^{18}O_2$ difference spectra of the MMOH$^{red}$/MMOB reaction with $O_2$ at pH 7.0, 4 °C and $\Delta t \approx 3.0$ s. Bottom, $^{16}O_2$ – $^{18}O_2$ difference spectra of the oxygenated buffers in the absence of MMOH and MMOB proteins. Intensities of sMMO spectra were normalized to protein vibration. In the absence of protein, relative intensity was normalized using buffer vibrations.

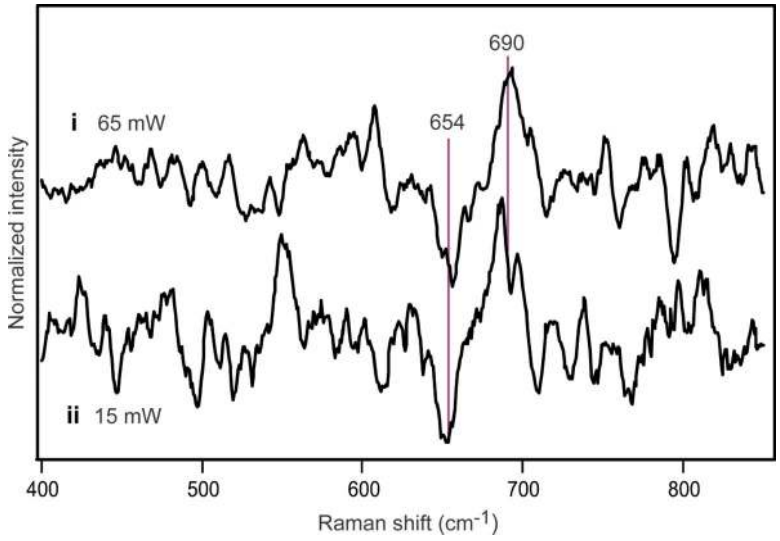


**Extended Data Figure 3. Power dependence of TR$^3$ spectra of sMMO**

$^{16}O_2$ – $^{18}O_2$ difference spectra obtained using 65 mW (i) and 15 mW (ii) excitation laser power show the same normalized intensity of oxygen vibrations in **Q**, indicating that no detectable photodecomposition is taking place under current conditions.

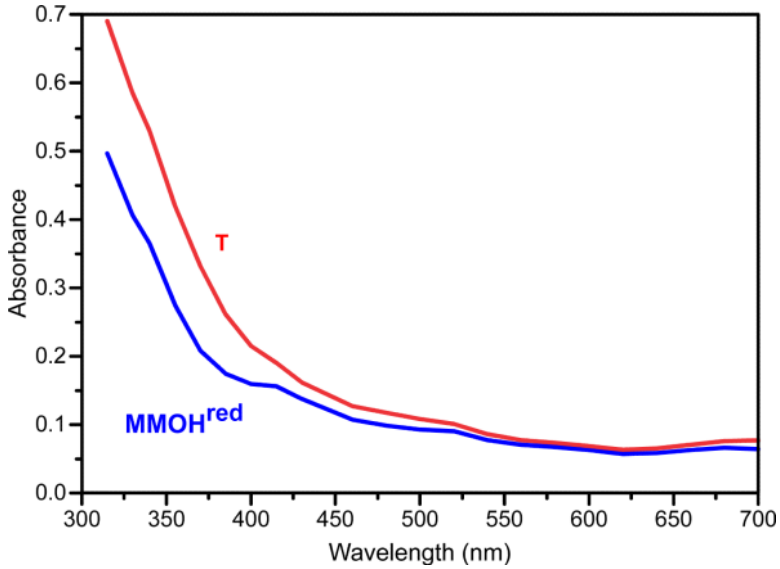


**Extended Data Figure 4. A comparison of the electronic absorption spectra of compound T (red trace) and MMOH$^{red}$ (blue trace)**

**T** exhibits an absorption band in the near-ultraviolet region, giving rise to its resonance Raman enhancement. Single wavelength time courses of the reaction of 25 μM MMOH$^{red}$/ MMOB with a 450 μM solution of $CH_4$ and 450 μM $O_2$ at 4 °C, pH 7 were recorded throughout the visible region (concentrations after mixing). The absorbance at each wavelength at the time of maximal **T** formation given by the speciation plot shown in Extended Data Fig. 1b was extracted and used to make the red trace shown.

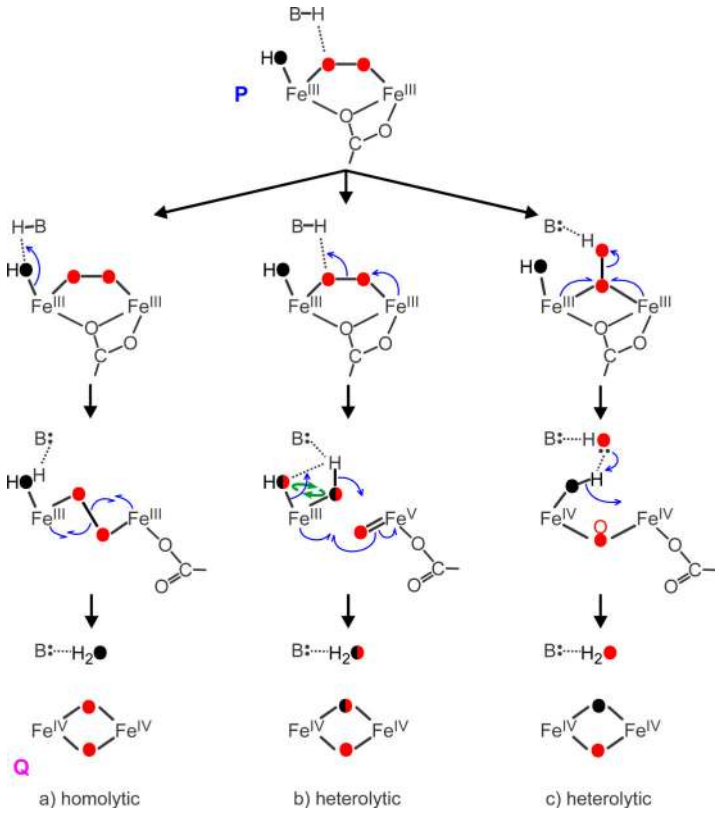


**Extended Data Figure 5. Potential O-O bond cleavage mechanisms in the dinuclear centre of MMO**

The most divergent mechanisms are shown along with expected isotopic composition of oxygen derived from $O_2$ (red) and solvent (black). All mechanisms are triggered by proton-dependent rearrangement of **P**[10,33]. The monodentate carboxylate bridge (E243) found in the diferrous enzyme[34] is likely to maintain this position in **P**, but return to the non-bridging position in **Q**, as found in the resting enzyme, to accommodate the diamond core structure. The catalytic base B, which mediates proton dependency, has not been definitively identified. Based on structural similarity to other di-iron $O_2$-activating enzymes and DFT computations for **P-**analogues in those systems[11,35,36], we have proposed[11] that E114 (a ligand to solvent-coordinated iron in **P**), is this base. Other ligands not directly involved in cleavage are omitted for clarity (see Fig. 3). Equal intensities of **Q**-$^{16}O_2$ and **Q**-$^{18}O_2$ modes, and the absence of **Q**-$^{16}O^{18}O$ mode in Fig. 2c, (i) argue against isotope scrambling in **Q** formation. This and all other experimental results reported to date are in full accord with the nominally concerted homolytic cleavage mechanism. We postulate that the loss of E243 bridge facilitates the conversion of *cis*-μ-peroxo adduct in **P** to the *trans*-μ-peroxo conformation and the ensuing O-O bond cleavage (**a**) to form the diamond core structure detected here. This transition is supported by DFT computations[37]. In contrast, the stepwise, end-on heterolytic cleavage mechanism (**c**) (analogous to formation of compound I in cytochrome P450) leads to the mixed isotope cluster in **Q**-$^{18}O_2$ and can be ruled out. Heterolytic cleavage of *trans*-μ-peroxo is essentially isoelectronic to and experimentally indistinguishable from the homolytic mechanism (**a**). The proton-assisted heterolytic cleavage of *cis*-μ-peroxo bridge (**b**) cannot be ruled out yet, but several observations argue

against it. (1) We did not observe isotope scrambling (curved green arrows), which is expected upon formation of two terminal oxygenic ligands on the same iron. While scrambling may not occur if ligands are highly stabilized, structural basis for such putative stabilization is not apparent. Scrambling may also not be observed if formation of diamond core is fast following bond cleavage, in which case mechanism (**b**) becomes, in essence, a stepwise, proton-assisted homolytic cleavage, also indistinguishable from (**a**). (2) Two iron atoms in di-ferric **P** and di-ferryl **Q** are in the same oxidation states and in indistinguishable electronic environments[2,20]. Such symmetry is unfavourable for O-O bond polarization and charge separation in the $Fe^{III}/Fe^{V}$ state during heterolytic cleavage. The deprotonated state of the peroxo bridge in **P** also argues against overall polarity of the site that would aid heterolytic cleavage.

**Extended Data Table 1**

Additional vibrational modes of metal centres relevant to Q and T

| Vibrational structure | System | $\nu(\Delta^{18}O)$ $cm^{-1}$ | $\nu^{16}O^{18}O$ $cm^{-1}$ | $\Delta^{2}H$ $cm^{-1}$ | Ref |
|---|---|---|---|---|---|
| | **sMMO Q** | 690 (−36) | 673 | 0 | This work |
| | **sMMO T** | 556 (−23) | - | 0 | This work |
|  | $[Fe^{IV}(O)(TMG_3tren)]$ | 843 (−33) | - | - | 38 |
| | TauD-F4 | 825 (−37) | - | 0 | 12 |
| | $[Fe^{IV}(O)(TMC)(NCCH_3)]^{2+}$ | 834 (−34) | - | - | 39 |
| 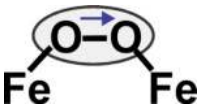 | $hDOHH_{peroxo}$ | 855[a] (−44) | 833 | - | 15 |
| | Peroxo-$\Delta^9$D | 898 (−53) | 874 | - | 40 |
| | Frog M ferritin peroxo | 851 (−51) | - | - | 41 |
| 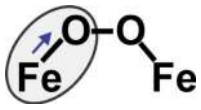 | $hDOHH_{peroxo}$ | 473 (−16) | 465 | - | 15 |
| | Peroxo-$\Delta^9$D | 442 (−17) | 433 | - | 40 |
| | Frog M ferritin peroxo | 485 (−17) | 477 | - | 41 |

References 38-41 are cited in this Table.

[a] represents the center of a Fermi Doublet

## Acknowledgements

We thank G. T. Babcock (deceased), S.-K. Lee and J. C. Nesheim (deceased) for initial studies that led to this project and E. Bergeron for technical assistance. This work was supported by the NIH grants GM40466 and GM100943 (to J.D.L.) and grant GM096132 (to D.A.P.).

## References


1. Lee SK, Nesheim JC, Lipscomb JD. Transient intermediates of the methane monooxygenase catalytic cycle. J. Biol. Chem. 1993; 268:21569–21577. [PubMed: 8408008]
2. Lee SK, Fox BG, Froland WA, Lipscomb JD, Münck E. A transient intermediate of the methane monooxygenase catalytic cycle containing a $Fe^{IV}Fe^{IV}$ cluster. J. Am. Chem. Soc. 1993; 115:6450–6451.
3. Shu L, et al. An $Fe^{IV}{}_2O_2$ diamond core structure for the key intermediate Q of methane monooxygenase. Science. 1997; 275:515–518. [PubMed: 8999792]
4. Dunietz BD, et al. Large scale ab initio quantum chemical calculation of the intermediates in the soluble methane monooxygenase catalytic cycle. J. Am. Chem. Soc. 2000; 122:2828–2839.
5. Han WG, Noodleman L. Structural model studies for the high-valent intermediate Q of methane monooxygenase from broken-symmetry density functional calculations. Inorganica Chim. Acta. 2008; 361:973–986. [PubMed: 19262682]
6. Siegbahn PEM. O–O bond cleavage and alkane hydroxylation in methane monooxygenase. J. Biol. Inorg. Chem. 2001; 6:27–45. [PubMed: 11191221]
7. Xue G, et al. A synthetic precedent for the $[Fe^{IV}{}_2(\mu\text{-}O)_2]$ diamond core proposed for methane monooxygenase intermediate Q. Proc. Natl Acad. Sci. USA. 2007; 104:20713–20718. [PubMed: 18093922]
8. Nesheim JC, Lipscomb JD. Large isotope effects in methane oxidation catalyzed by methane monooxygenase: evidence for C–H bond cleavage in a reaction cycle intermediate. Biochemistry. 1996; 35:10240–10247. [PubMed: 8756490]
9. Liu KE, et al. Spectroscopic detection of intermediates in the reaction of dioxygen with the reduced methane monooxygenase hydroxylase from *Methylococcus capsulatus* (Bath). J. Am. Chem. Soc. 1994; 116:7465–7466.
10. Tinberg CE, Lippard SJ. Revisiting the mechanism of dioxygen activation in soluble methane monooxygenase from *M. capsulatus* (Bath): evidence for a multi-step, proton-dependent reaction pathway. Biochemistry. 2009; 48:12145–12158. [PubMed: 19921958]
11. Banerjee R, Meier KK, Münck E, Lipscomb JD. Intermediate P* from soluble methane monooxygenase contains a diferrous cluster. Biochemistry. 2013; 52:4331–4342. [PubMed: 23718184]
12. Grzyska PK, Appelman EH, Hausinger RP, Proshlyakov DA. Insight into the mechanism of an iron dioxygenase by resolution of steps following the $Fe^{IV}$=O species. Proc. Natl Acad. Sci. USA. 2010; 107:3982–3987. [PubMed: 20147623]
13. Zheng H, Lipscomb JD. Regulation of methane monooxygenase catalysis based on size exclusion and quantum tunneling. Biochemistry. 2006; 45:1685–1692. [PubMed: 16460015]
14. Hohenberger J, Kallol R, Meyer KK. The biology and chemistry of high-valent iron–oxo and iron–nitrido complexes. Nat. Commun. 2012; 3:720. [PubMed: 22395611]
15. Vu VV, et al. Human deoxyhypusine hydroxylase, an enzyme involved in regulating cell growth, activates $O_2$ with a nonheme diiron center. Proc. Natl Acad. Sci. USA. 2009; 106:14814–14819. [PubMed: 19706422]
16. Shiemke AK, Loehr TM, Sanders-Loehr J. Resonance Raman study of oxyhemerythrin and hydroxhemerythrin: evidence for hydrogen bonding of ligands to the Fe-O-Fe center. J. Am. Chem. Soc. 1986; 108:2437–2443. [PubMed: 22175597]
17. Stone KL, Behan RK, Green MT. Resonance Raman spectroscopy of chloroperoxidase compound II provides direct evidence for the existence of an iron(IV)-hydroxide. Proc. Natl Acad. Sci. USA. 2006; 103:12307–12310. [PubMed: 16895990]
18. Momenteau M, Reed CA. Synthetic heme dioxygen complexes. Chem. Rev. 1994; 94:659–698.
19. Wilkinson EC, et al. Raman signature of the $Fe_2O_2$ "diamond" core. J. Am. Chem. Soc. 1998; 120:955–962.
20. Tinberg CE, Lippard SJ. Dioxygen activation in soluble methane monooxygenase. Acc. Chem. Res. 2011; 44:280–288. [PubMed: 21391602]

21. Poulos TL. Heme enzyme structure and function. Chem. Rev. 2014; 114:3919–3962. [PubMed: 24400737]
22. Tolman WB. Making and breaking the dioxygen O-O bond: new insights from studies of synthetic copper complexes. Acc. Chem. Res. 1997; 30:227–237.
23. Collman JP, Dey A, Yang Y, Ghosh S, Decreau RA. $O_2$ reduction by a functional heme/nonheme bis-iron NOR model complex. Proc. Natl Acad. Sci. USA. 2009; 106:10528–10533. [PubMed: 19541624]
24. Xue G, De Hont R, Münck E, Que L Jr. Million-fold activation of the [$Fe_2(\mu\text{-}O)_2$] diamond core for C-H bond cleavage. Nat. Chem. 2010; 2:400–405. [PubMed: 20414242]
25. Zheng H, Zang Y, Dong Y, Young VG Jr, Que L Jr. Complexes with $Fe^{III}_2(\mu\text{-}O)(\mu\text{-}OH)$, $Fe^{III}2(\mu\text{-}O)_2$, and [$Fe^{III}_3(\mu_2\text{-}O)_3$] cores: Structures, spectroscopy, and core interconversions. J. Am. Chem. Soc. 1999; 121:2226–2235.
26. Sjöberg B-M, Loehr TM, Sanders-Loehr J. Raman spectral evidence for a μ-oxo bridge in the binuclear iron center of ribonucleotide reductase. Biochemistry. 1982; 21:96–102. [PubMed: 7037052]
27. Fox BG, Shanklin J, Ai J, Loehr TM, Sanders-Loehr J. Resonance Raman evidence for an Fe-O-Fe center in stearoyl-ACP desaturase. Primary sequence identity with other diiron-oxo proteins. Biochemistry. 1994; 33:12776–12786. [PubMed: 7947683]
28. Carter EL, Proshlyakov DA, Hausinger RP. Apoprotein isolation and activation, and vibrational structure of the *Helicobacter mustelae* iron urease. J. Inorg. Biochem. 2012; 111:195–202. [PubMed: 22196017]
29. Sitter AJ, Shifflett JR, Terner J. Resonance Raman spectroscopic evidence for heme iron-hydroxide ligation in peroxidase alkaline forms. J. Biol. Chem. 1988; 263:13032–13038. [PubMed: 3417650]
30. Zhang J, Lipscomb JD. Role of the C-terminal region of the B component of Methylosinus trichosporium OB3b methane monooxygenase in the regulation of oxygen activation. Biochemistry. 2006; 45:1459–1469. [PubMed: 16445288]
31. Fox BG, Froland WA, Dege JE, Lipscomb JD. Methane monooxygenase from Methylosinus trichosporium OB3b. Purification and properties of a three-component system with high specific activity from a type II methanotroph. J. Biol. Chem. 1989; 264:10023–10033. [PubMed: 2542319]
32. Brazeau BJ, Lipscomb JD. Kinetics and activation thermodynamics of methane monooxygenase compound Q and reaction with substrates. Biochemistry. 2000; 39:13503–13515. [PubMed: 11063587]
33. Lee SK, Lipscomb JD. Oxygen activation catalyzed by methane monooxygenase hydroxylase component: Proton delivery during the O-O bond cleavage steps. Biochemistry. 1999; 38:4423–4432. [PubMed: 10194363]
34. Rosenzweig AC, Nordlund P, Takahara PM, Frederick CA, Lippard SJ. Geometry of the soluble methane monooxygenase catalytic diiron center in two oxidation states. Chem. Biol. 1995; 2:409–418.
35. Srnec M, et al. Structural and spectroscopic properties of the peroxodiferric intermediate of Ricinus communis soluble $\Delta^9$ desaturase. Inorg. Chem. 2012; 51:2806–2820. [PubMed: 22332845]
36. Jensen KP, Bell CB III, Clay MD, Solomon EI. Peroxo-type intermediates in class I ribonucleotide reductase and related binuclear non-heme iron enzymes. J. Am. Chem. Soc. 2009; 131:12155–12171. [PubMed: 19663382]
37. Han WG, Noodleman L. Structural model studies for the peroxo intermediate P and the reaction pathway from P→Q of methane monooxygenase using broken-symmetry density functional calculations. Inorg. Chem. 2008; 47:2975–2986. [PubMed: 18366153]
38. England J, et al. A synthetic high-spin oxoiron(IV) complex: Generation, spectroscopic characterization, and reactivity. Angew. Chem. Int. Ed. 2009; 48:3622–3626.
39. Rohde J-U, et al. Crystallographic and spectroscopic characterization of a nonheme Fe(IV)=O complex. Science. 2003; 299:1037–1039. [PubMed: 12586936]
40. Broadwater JA, Ai J, Loehr TM, Sanders-Loehr J, Fox BG. Peroxodiferric intermediate of stearoyl-acyl carrier protein $\Delta^9$ desaturase: Oxidase reactivity during single turnover and

implications for the mechanism of desaturation. Biochemistry. 1998; 37:14664–14671. [PubMed: 9778341]

41. Moenne-Loccoz P, et al. The ferroxidase reaction of ferritin reveals a diferric μ-1,2 bridging peroxide intermediate in common with other $O_2$-activating non-heme diiron proteins. Biochemistry. 1999; 38:5290–5295. [PubMed: 10220314]

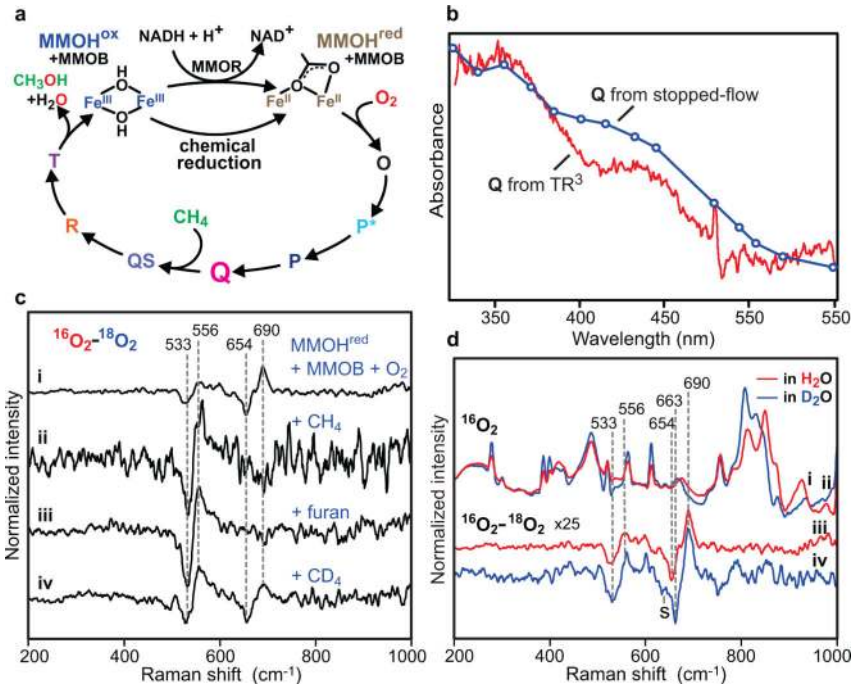


**Figure 1. Reaction of sMMO with $O_2$**

**a**, The catalytic cycle includes stable $MMOH^{ox}$ and $MMOH^{red}$ and detectable transient species **O**, **P***, **P**, **Q** and **T**; transient states **QS** and **R** were predicted from kinetic, spectroscopic, and chemical studies. **b**, An *in situ* transient difference electronic absorption spectrum of the reaction mixture (vs anaerobic $MMOH^{red}$) in the $TR^3$ instrument at $\Delta t \approx 3.0$ s (red, $1.0 \times 0.1^2$ mm probe volume) in comparison with spectrum of **Q** reconstructed from stopped-flow kinetic traces (markers, blue). **c**, Transient $^{16}O_2 - {}^{18}O_2$ difference resonance Raman spectra of sMMO reveal vibrations of iron-bound oxygen atoms. Measurement conditions: pH 7.0, 4 °C, $\Delta t \approx 3.0$ s. Spectra recorded without the substrate (i) show marked changes when 0.45 mM $CH_4$ (ii), 3.5 mM furan (iii) or 0.45 mM $CD_4$ (iv) is added. **d**, Solvent vibrations in the absolute resonance Raman spectra are sensitive to $H_2O$ (i)/$D_2O$ (ii) substitution. $^{16}O_2 - {}^{18}O_2$ difference spectra of sMMO recorded in $H_2O$ (iii) show little sensitivity to $D_2O$ (iv) substitution. The upshift of $^{18}O$ vibration of **Q** and the appearance of a low-frequency shoulder (marked with S) in $D_2O$ is attributed to Fermi resonance with a protein-derived metal ligand.

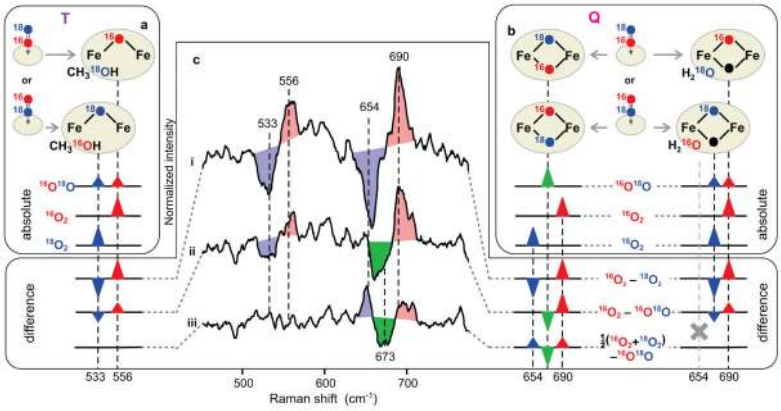


**Figure 2. Fingerprinting cluster structure using $^{16}O^{18}O$ mixed oxygen isotope**

**a**, **b**, Asymmetrically labelled $^{16}O^{18}O$ can initially bind in two equiprobable orientations, yielding an even mixture of two isotopomers in **T** or **Q** (panels **a** and **b**, top) exhibiting characteristic vibrations (panels **a** and **b**, bottom). Two scenarios are possible for **Q**, depending on whether two (left) or one (right) $O_2$-derived atoms (red and blue) are incorporated into the cluster. If only one atom is incorporated, then the second oxygen atom in the core structure would derive from solvent (black). Water and methanol exemplify a departing oxygen atom while other ligands are omitted for simplicity. Since the two

isotopomers of **T** (**a**) and those of singly labelled **Q** (**b**, right) have identical composition as corresponding $^{16}O_2$ and $^{18}O_2$ derivatives, they will exhibit both vibrations simultaneously at half the intensity. Doubly labelled **Q** (panel **b**, left) will be different from both symmetrically labelled derivatives and thus, **c**, will exhibit a new vibration (green), as illustrated by isotope difference spectra (**c**). The $^{16}O_2 - {}^{16}O^{18}O$ difference (ii) in singly labelled cluster (**a**, **b** right) will appear as the $^{16}O_2 - {}^{18}O_2$ difference (i) with reduced intensity. The $^{16}O^{18}O$ derivative will be identical to the average of symmetrical isotopomers, yielding no signal in trace iii, as observed experimentally for **T**. The new frequency in doubly labelled **Q** should appear in both difference (ii) and (iii), and can, indeed, be seen in experimental data at 673 $cm^{-1}$. Spectral superimposition inflates the apparent isotopic shift when frequencies of isotopomers are close (traces (ii) and (iii), right), but not when bands are well separated (trace (i)).

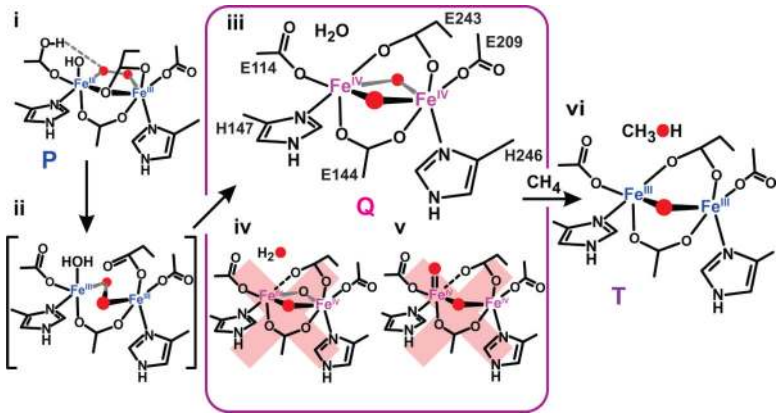


**Figure 3. Formation of compound Q and its reaction with methane**

Homolytic mechanism of O-O bond cleavage (ii) upon formation of **Q** from **P** (i) follows from the structure of **Q** (iii) presented here. Alternative structures of **Q** (iv, v) discounted by current results are also shown. The iron shown on the left in the **Q** structure (iii) may retain the solvent found in **P**. In this case, E243 would not bind to this iron, but would be likely to hydrogen bond with the bound solvent[4,5]. **T** (vi) contains a single atom from $O_2$ while another is incorporated in the product.

## Table 1

Vibrational modes of metal centers relevant to Q and T

| Vibrational structure | System | $\nu(\Delta^{18}O)$ $cm^{-1}$ | $\nu^{16}O^{18}O$ $cm^{-1}$ | $\Delta^{2}H$ $cm^{-1}$ | Ref. |
|---|---|---|---|---|---|
| 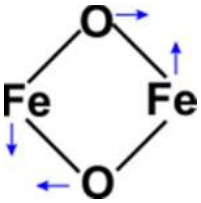 | [4-OMe-3,5-Me-TPA$Fe^{IV}$(μ-O)]$_2$ | 674 (−30) | 665 | - | 7 |
| | [$(TPA)_2Fe^{III}$(μ-O)2$Fe^{IV}$] | 666 (−28)* | 644 | - | 19 |
| | [$(5\text{-Me-TPA})_2Fe^{3+}(\mu\text{-O})_2Fe^{IV}$] | 668 (−32) | - | - | 19 |
| | sMMO **Q** | 690 (−36) | 673 | 0 | This work |
| | sMMO **T** | 556 (−23) | - | 0 | This work |
| 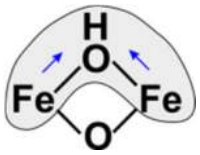 | [$Fe_2(\mu\text{-O})(\mu\text{-OH})(4,6\text{-Me}_6\text{-TPA})_2]^{III}$ | 497 (−13) | - | −3 | 25 |
| | [$Fe_2$-(μ-O)(μ-OH)$(BPEEN)_2]^{III}$ | 504 (−16) | | −4 | 25 |
| 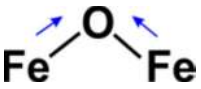 | Ribonucleotide reductase-R2 | 496 (−15) | - | 0 | 26 |
| | $\Delta^9$-desaturase | 519 (−18) | - | 0 | 27 |
| | Urease UreA2B2 | 497 (−21) | - | - | 28 |
|  | Hydroxomet-hemerythrin | 565 (−27) | - | −5 | 16 |
| | Chloroperoxidase Compound-II | 565 (−22) | - | −13 | 17 |
| | Horseradish peroxidase | 503 (−19) | - | +6 | 29 |

‡ Additional cases are considered in references 12, 15 and as noted in Extended Data Table 1.

* represents center of a Fermi Doublet